Nondestructive testing by using long-wave infrared interferometric techniques with CO_2 lasers and microbolometer arrays

Igor Alexeenko,[1,4] Jean-François Vandenrijt,[2] Giancarlo Pedrini,[1] Cédric Thizy,[2] Birgit Vollheim,[3] Wolfgang Osten,[1] and Marc P. Georges[2,*]

[1]Institut für Technische Optik—Universität Stuttgart, Pfaffenwaldring 9, Stuttgart 70569, Germany

[2]Centre Spatial de Liège—Université de Liège, Avenue du Pré Aily, B-4031 Angleur (Liège), Belgium

[3]InfraTec GmbH, Gostritzer Strasse 61-63, Dresden 01217, Germany

[4]Current address: Immanuel Kant Baltic Federal University, A. Nevskogo Street 14, Kaliningrad 236041, Russia

*Corresponding author: mgeorges@ulg.ac.be

Received 6 July 2012; revised 20 September 2012; accepted 20 September 2012; posted 21 September 2012 (Doc. ID 171765); published 22 October 2012

We describe three different interferometric techniques (electronic speckle pattern interferometry, digital holographic interferometry, and digital shearography), using a long-wave infrared radiation produced by a CO_2 laser and recorded on a microbolometer array. Experimental results showing how these methods can be used for nondestructive testing are presented. Advantages and disadvantages of these approaches are discussed. © 2012 Optical Society of America

OCIS codes: 090.2880, 120.6165, 120.4290.

1. Introduction

Methods based on holographic interferometry (HI) [1] and electronic speckle pattern interferometry (ESPI) [2] are commonly used for nondestructive testing (NDT) of mechanical structures and dynamic analysis. These techniques are based on the comparison of wavefronts recorded at different instants. The result of the wavefront comparison is the phase difference containing the information about the object deformation during the recording.

There are many publications describing results obtained by HI and ESPI using visible or ultraviolet light; however, few investigations in the long-wave infrared (LWIR) spectral range (wavelength 8–14 μm) were realized up to now.

The main reasons for the limited number of LWIR interferometric developments are that working at such wavelength requires (1) specific optical elements usually made of germanium (Ge) or zinc selenide (ZnSe), (2) an adequate hologram recording medium with good performance, (3) imagers sensitive in that range, and (4) a laser emitting in that range. The laser that we consider here is a single longitudinal mode CO_2 laser, which can be found with power of several watts at low prices compared to lasers with similar power in the visible range. With the growth of the thermal-imaging systems market, optical components can be found in stock at affordable cost as well. At last, various thermal imager technologies exist with an increasing number of pixels, and the uncooled microbolometer arrays [3] offer now advantages in terms of ease of use, affordable costs, and state-of-the-art megapixel format [4]. Therefore, it can be envisaged to build LWIR interferometric NDT systems, which can offer several advantages over their visible equivalents. The advantage of LWIR techniques is that the displacement measurement range is increased because it is

1559-128X/13/010A56-12$15.00/0

directly proportional to the laser wavelength. Also, the sensitivity of the holographic setup to external perturbations, which is driven by various factors related to the object and the setup mechanical stiffness, are lower in LWIR than in the visible range. Indeed, the fringe pattern formed by interference of reference and object beams at the holographic photosensitive medium must not move by more than a tenth of wavelength during capture.

Nevertheless the important question about the holographic recording medium remains, which was already addressed in the past for the case of LWIR photosensitive plates. Let us cite the early works by Chivian *et al.*, who used a thermochromic material for recording at 10.6 μm and readout along with a He–Ne laser [5]. These works were followed by other groups using the same separated wavelengths for the recording and readout steps but applied to other recording media such as liquid crystals [6], wax and gelatin films [7], or other recording schemes with cuprous mercuric iodide [8]. In the same period, a Canadian group made a lot of investigations considering several materials and presented applications with acrylic and thin films [9], wax [10,11], oil films deposited on glass plates [12], photoresists [13], and poly (acrylic acid) films [14]. Until now, there is no evidence of high-quality holographic interferograms based on such materials and arrangements. An alternative to chemical photosensitive materials is the electronic recording of interference patterns formed by object and reference beams in various configurations, which rely either on ESPI or digital holography [15]. ESPI with a CO_2 laser was first introduced by Løkberg and Kwon in 1984 [16], who used pyroelectric vidicon cameras. Although of major interest for its novelty, the paper reports the critical behavior of the vidicon cameras, which react to changes of the radiation energy. This was a major drawback, and the authors were obliged to modulate the intensity of light to record the speckle patterns. For that reason they only showed application of LWIR ESPI on vibrating objects.

More recently Allaria *et al.* [17] introduced LWIR digital holographic reconstruction of a small mask object in a Mach–Zehnder configuration. The holograms were recorded directly on a modern version of a pyroelectric thermal imager equipped with an internal chopper for coping with stationary image intensities. Other works followed by the same group with the same sensor and with the aim of shape measurement [18].

In our work we consider microbolometer arrays for the reasons discussed earlier and because they do not require artificial variations of light beams. Recently George *et al.* showed digital holography based on a microbolometer array [19] with an optical setup similar to that of [17,18].

Recently we have proposed several setups using electronic recording of holograms and specklegrams with microbolometer arrays and a CO_2 laser for applications in interferometry of scattering objects, more specifically in-plane displacement measurements by ESPI [20] and out-of-plane displacement by both ESPI and lensless digital HI (DHI) [21]. The results presented there were obtained with early microbolometer technologies with small formats (320 × 240 pixels) and with the purpose of demonstrating the capabilities of LWIR holography techniques in applications of displacement measurement. The objects considered in these papers were metallic plates mounted on rotation stages, with countermeasurement techniques for cross-correlation of obtained values.

In [21] we discussed the problem of the specularity of the surface in the LWIR range. Following Yamaguchi [22], the surface becomes completely scattering and speckle appears when the laser wavelength is smaller than the surface roughness. On the other side, specular reflection appears as soon as the wavelength is larger than the roughness and quickly dominates the speckle pattern intensity. Nevertheless, to some extent the speckle pattern can still be observed, but its intensity is smaller than the specular peak. With metallic objects, the surface often presents a roughness such that it reflects in a specular way. We circumvented this by using a white removable powder, which increases the roughness in such a way that objects scatters enough to create the necessary speckle.

The purpose of the current paper is to show further developments in the field of NDT of aeronautical composite structures with various constructions, defects, and surface characteristics. We had a series of representative samples made of glass-fiber-reinforced plastic (GFRP), carbon-fiber-reinforced plastic (CFRP), and Kevlar. Ideally these structures need to be investigated on the production site, aiming at flaw detection or assessment of mechanical behavior (displacement measurement) under loads. Our first step in this project was to assess the roughness of these samples, and we showed that most of the above cited materials have a roughness that is high enough to generate speckle with CO_2 lasers [23]. Preliminary DHI experiments were already reported with these samples [24].

In this paper, we present three techniques of interest for NDT that we extended to LWIR with a CO_2 laser. On one hand we have a first category that concerns measurement of displacement fields, namely ESPI and DHI, and on another hand we have digital shearography (DS), which allows measuring the derivative of displacements along one particular direction (strain).

The two former are studied on the basis of a similar setup because of the high similarity of optical schemes, with Section 2 being devoted to ESPI and Section 3 to DHI. Section 4 presents developments and results with DS.

2. LWIR Electronic Speckle Pattern Interferometry

A. Setup and Technique Description

Figure 1 shows the scheme of the ESPI setup. It includes (1) a CO_2 laser (from VM-TIM) with wavelength $\lambda = 9.3$ or 10.6 μm (selectable by the user),

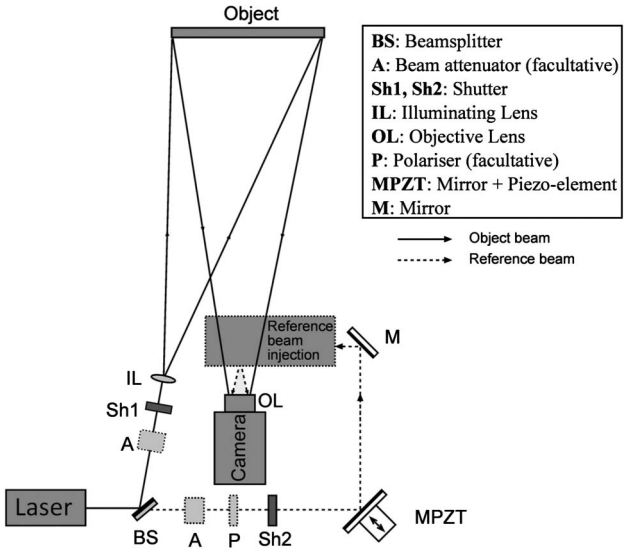

Fig. 1. Scheme of the LWIR ESPI setup.

20 m coherence length, 1.6 mm beam diameter at the laser output, beam divergence of 8.7 mrad, power up to 8 W, and linear polarization; (2) an uncooled microbolometer infrared camera (VarioCAM-hr, from Jenoptik) with 640 × 480 pixels of size 25 μm × 25 μm (giving a detector size of 16 mm × 12 mm), a dynamic range of 16 bits, and a frame rate of 50 frames/s, running with IRBIS software by Infratec GmbH. The objective lens (OL) of the camera module has a 50 mm focal length, is made of germanium, and is especially designed for thermography in order to provide maximal resolution and field of view.

As we will explain later, we have not detached the OL from the camera to incorporate the reference beam. The camera is equipped with an internal aperture wheel, which is located between the objective and the sensor and has two positions: a closed position that is necessary for automated internal recalibration of the camera from time to time (necessary in thermography application) and a fully open position with diameter $D = 21$ mm, which constitutes the aperture stop (AS) of the OL. The distance between the aperture and the sensor is $L = 21$ mm. The lateral speckle size d_{sp} can be found by the diffraction theory: it is given by separation of the first two minima of the first-order Bessel function J_1 and is expressed as $d_{sp} = 2.44\lambda L/D = 22.7$ or 26 μm as a function of the laser wavelength used. Because the speckle size is smaller than (or barely identical to) the pixel size of the LWIR detector, speckle grains are not fully resolved. Due to the fact that the aperture diameter is fixed for LWIR systems, one cannot change the L/D ratio for making speckle grains resolvable. However, Maack *et al.* [25] have already shown that ESPI can be performed under such circumstances. Their works were carried out under visible light, and we extended this discussion in our earlier works to LWIR ESPI [21].

The implementation of ESPI requires that the laser beam is split in two parts. The first one (object beam, represented by solid lines) illuminates the object, which scatters light towards the camera. The second part is the reference beam (dotted lines) that is arranged to enter the camera through a reference-beam injection setup that is discussed in the next section.

The reference and speckle object beams can be represented by their electric field vectors, respectively $\boldsymbol{R}(x,y) = R(x,y)\boldsymbol{e_R}\exp(i\varphi_R(x,y))$ and $\boldsymbol{U}(x,y) = U(x,y)\boldsymbol{e_U}\exp(i\varphi_U(x,y))$. Their interference at each point (x,y) of the detector produces an intensity pattern (speckle gram), which is given by

$$I(x,y) = |\boldsymbol{R}(x,y)|^2 + |\boldsymbol{U}(x,y)|^2 + \boldsymbol{R}(x,y)\boldsymbol{U}^*(x,y) + \boldsymbol{R}^*(x,y)\boldsymbol{U}(x,y), \tag{1a}$$

$$= I_R(x,y) + I_U(x,y) + (\boldsymbol{e_R}\boldsymbol{e_U})2(I_R(x,y)I_U(x,y))^{1/2} \times\cos(\phi(x,y)), \tag{1b}$$

where $I_R(x,y) = |\boldsymbol{R}(x,y)|^2$ and $I_U(x,y) = |\boldsymbol{U}(x,y)|^2$ are respectively the intensities of reference and object beams at the sensor level, $\boldsymbol{e_R}$ and $\boldsymbol{e_U}$ are the unit vectors giving the orientation of their electric field vector, and $\varphi_R(x,y)$ and $\varphi_U(x,y)$ are their intrinsic phase and their relative phase difference, defined by $\phi(x,y) = \varphi_R(x,y) - \varphi_U(x,y)$. As is commonly known, in any interferometric setup the contrast of interference, given by $m(x,y) = \boldsymbol{e_R}\boldsymbol{e_U}2(I_R(x,y)I_U(x,y))^{1/2}/(I_R(x,y) + I_U(x,y))$, is maximized when the polarizations are parallel ($\boldsymbol{e_R}\boldsymbol{e_U} = 1$) and when $I_R(x,y) = I_U(x,y)$.

Therefore one has to ensure that both conditions can be made possible in the setup. One unknown is the polarization behavior of the samples that are observed. As mentioned earlier, the latter are made of CFRP, GFRP, and Kevlar. In previous experiments [21] we also proposed the use of white removable powder (developer powder for liquid penetrant technique) in order to increase the roughness when the latter is too small to generate speckles. In the case of the above mentioned materials, as well as with the developer powder, we have observed that the scattered beam is globally linearly polarized, with a small depolarization (not exceeding 10%). It is worth mention that, at least in the case of the white developer powder, the polarization behavior is totally different than when illuminated with a visible laser, which completely depolarizes light. Therefore it was important to consider these aspects in the design of the LWIR ESPI setup because a highly depolarized object beam would require a polarizer in front of the camera for interfering with the reference beam in order to limit background noise. Indeed, such a noise can be represented by a supplementary intensity term in Eq. (1), which further limits the interference contrast. In our case, a preserved object-beam polarization did require the use of such a polarizer. However, it is still necessary to try equalizing the intensities of beams as much as possible by

adequate components at the level of beam separation. The separation is generally ensured by beam splitters (BSs), which are made of ZnSe glass with coating that allows either an equal ratio, that is, reflection and transmission of 50% (R50/T50), or asymmetric ones. Various solutions were used in the setup, and the results presented later make use of one or another of those we will describe now. The first one uses a R50/T50 BS from ULO Optics. Because a low level of light is scattered by the object towards the camera, a R50/T50 BS induces a reference beam much more intense than the object when reaching the camera sensor. Therefore attenuators (A) need to be placed in both arms to finely adjust the contrast. These attenuators are made of two polarizers of which the transmission axes are rotated one to another. Therefore their output polarizer also plays the role of correctly orienting the polarization of both beams. The second possibility used for the beam splitting is to consider an asymmetric-ratio BS: R90/T10 or R99/T1, manufactured by II-VI Company. In this case, the reference-beam intensity is intrinsically small and better matches the scattered object-beam intensity. However, it was still too high and required a fine adjustment for beam ratio closer to unity. For that purpose we used a polarizer (P) in the reference beam, which allows adjusting its intensity, the laser beam being polarized. Despite the fact that we changed the polarization direction of the reference beam ($\boldsymbol{e_R}\boldsymbol{e_U} < 1$), the polarizer transmission direction was very close to the laser polarization and this had no large influence on the final interference contrast.

After the BS, the object beam is rendered diverging by means of a ZnSe illumination lens (IL), of which the focal length is chosen to illuminate the whole object surface. The reference beam is travelling towards the reference injection setup. On its path, a set of folding mirrors are placed, one of them (MPZT) being mounted on a piezotranslator (Physical Instruments, P-611.1S, closed loop). The movement of the latter allows changing the path length in the reference arm in order to implement the phase-shifting technique, which is necessary to determine the phase of the wavefront.

During the acquisition of the specklegrams, the camera is synchronized with the phase shifting of the piezo element: a set of four images is recorded for positions of the MPZT mirror that induce a $\pi/2$ phase shift between each acquisition. Therefore the phase-shifted specklegrams are expressed as follows (leaving aside the (x,y) dependency for a matter of simplicity):

$$I_n = I_R + I_U + m(I_R + I_U)\cos\left(\phi + n\frac{\pi}{2}\right), \quad (2)$$

with $n = 1, 2, 3, 4$. Eq. (2) is used to calculate the phase according to the well-known four-buckets algorithm: $\phi = \tan^{-1}[(I_4 - I_2)/(I_1 - I_3)]$. If we record two such sets of four specklegrams $I_{n,a}$ and $I_{n,b}$ for two states of the object, noted a and b, we can compute their phases ϕ_a and ϕ_b. The phase difference $\Delta\phi = \phi_a - \phi_b$ can be related to the displacement $\boldsymbol{d}$ of each object point, imaged in each point of the camera (x,y). This relationship is given by

$$\Delta\phi = \frac{2\pi}{\lambda}\boldsymbol{s}\cdot\boldsymbol{d}, \quad (3)$$

where the sensitivity vector defined by $\boldsymbol{s} = \boldsymbol{k}_1 - \boldsymbol{k}_2$ is determined by the geometry of the setup, where $\boldsymbol{k}_1$ and $\boldsymbol{k}_2$ are the unit vectors of illumination and observation, respectively.

In Section 2.C we present a series of phase maps $\Delta\phi(x,y)$, which were obtained when composite samples undergo thermal loads. Before showing results, we have to explain an important part of the study, which is devoted to injection of the reference beam in the camera for producing the interference with the object beam and recording the specklegrams.

B. Injection of Reference Beam

The injection of the reference beam into the camera is ensured by a beam combination device, which is a key element for any ESPI setup and is usually placed between the imaging lens and the sensor. In visible light, such a beam combiner (BC) is often a BS cube, which transmits the object beam and reflects the reference beam. The reference beam is a diverging beam issued from a point source (e.g., from an optical fiber or a pinhole), which is conjugate to the limiting diaphragm of the imaging lens in the object arm.

In the design of a LWIR ESPI setup, we have to reach similar ideal conditions. Also we knew by experience that CO_2 laser beams can irreversibly destroy pixels of the microbolometer array. Therefore the study of the reference injection appeared as an important step of the development.

In our study we have analyzed the design of some OLs made for an uncooled LWIR camera in order to assess the feasibility of placing a BC between them and the focal plane array. The back focal distance available between our 50 mm focal length OL and the focal plane array is on the order of 20 mm. If we take into account the fact that there is a germanium window at a few millimeters in front of the sensor and that optical elements of the OL can move towards the sensor when adjusting the focus, there remains little space for placing a BC. We have also to consider that such uncooled infrared cameras have built-in aperture wheels out of the germanium window. In such aperture wheels a blocking aperture is present because the cameras have to be recalibrated from time to time to ensure good thermal measurement when used for thermography purposes.

For our development, we could have removed this device and built a new box for the sensor and electronics in order to have the sensor easily accessible for incorporating a BC. We already followed such an approach in our preliminary developments presented in [21]. Although those earlier results were encouraging, noisy images were obtained, which was partly

due to thermal noise coming from the environment of the sensor because the latter was not enclosed. In the new developments presented here, we definitely seek better-quality results with a state-of-the-art camera and OLs. Therefore we avoided dismantling our equipment in any way for incorporating optics. For that reason we studied the injection of the reference beam using different approaches that are described in the next section.

We know that we ideally need a spherical reference beam, which issues from the AS or diaphragm of the OL. The 50 mm OL considered here (and in general all the OLs made for uncooled cameras) have their AS after the last lens; moreover, it is attached to the aperture wheel inside the camera. In order to accurately study the injection of the reference beam, we need the OL design, but we were not allowed to obtain it from its manufacturer. Consequently, we measured some useful optical parameters, like the front and back focal distances, on a separate optical bench using a CO_2 laser collimated beam. We found that the front focal distance (between the first lens and the object focal point) is 17 mm, whereas the back focal distance (between the last lens and the image focal point) is 24 mm. Figure 2 shows a representation of the OL which has its AS a few millimeters away from the last lens of OL. The figure shows the ideal situation for the injection of the reference beam (dotted lines). With the OL parameters, we calculated that, in order to cover the whole detector, the injection lens L has to have a focal length of 252 mm and a diameter of 100 mm [26]. Such an ideal element is not in the catalog and has to be manufactured at high cost. Therefore we preferred alternative ways: either keeping the ideal requirement of centering the reference point source on the center of the AS (optimized configuration) or departing from it with simpler working configurations, admitting the possibility of lower quality of interference between reference and object beams.

A drawback of the frontal injection of the reference beam is the necessity of large BCs, which are essentially BSs similar to those already discussed in the previous section. Because the OL has a typical diameter of 50 mm, the BC must be typically 80 mm wide to avoid vignetting. Such a large element can be realized in ZnSe, but it is quite expensive. In order to find an alternative to such elements, we imagined to bring a point source in the middle of the AS through an optical fiber embedded in a modified medical needle. The needle biased aperture is sealed by a mirror, of which the reflecting face is turned inside (see Fig. 3). A 50 μm diameter hole was drilled on the upper part of the needle at an appropriate location. The beam launched by the LWIR fiber is then reflected by the mirror and exits the needle through that hole. The ensemble constitutes a very compact point source. The LWIR fiber is a hollow silica waveguide of 500 μm diameter and 1 m length manufactured by Polymicro Company.

Figure 4 shows various possibilities that were analyzed. Any configuration for injecting the reference beam must be such that the latter is large enough to cover the whole detector. Figure 4(a) consists in focusing the reference beam on the object focal point F of the OL. This way the reference beam is naturally collimated after having passed the OL and covers the entire detector (provide the injection lens is sufficiently large). Figure 4(b) is an alternative to the previous one and makes use of the modified needle described above. It is sufficient to place the needle point source at the object focal point F. Figure 4(c) is a further alternative that was also used with success. The LWIR fiber is used with a lens that focuses the beam well beyond the focal point F. A 40 μm diameter pinhole at the output of the fiber performs filtering. This allows obtaining a homogeneous beam, which is then passed through a ZnSe lens of 50 mm focal length and 50 mm diameter. The reference is not collimated anymore when reaching the detector but is slightly converging. In this case, the interference with the object beam is limited on a central part of the detector.

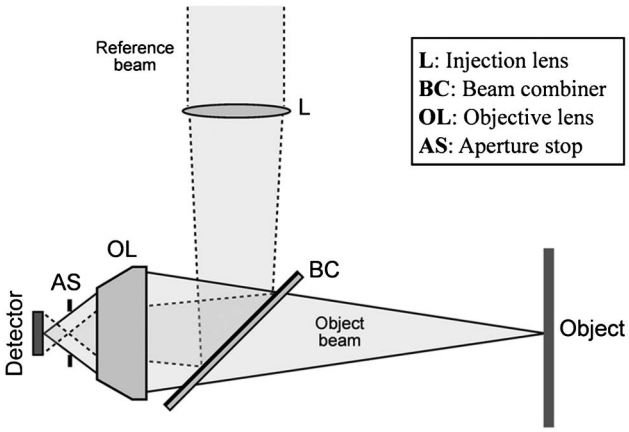

Fig. 2. Ideal reference beam injection.

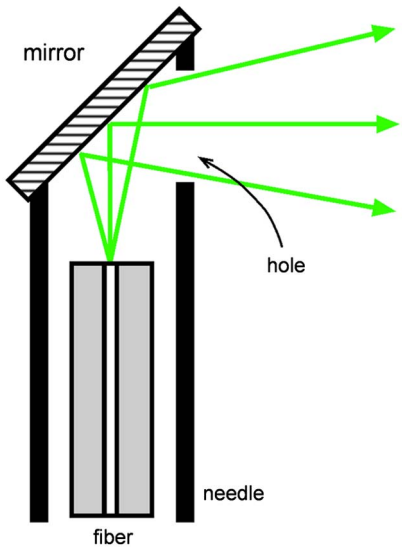

Fig. 3. (Color online) Modified needle with embedded LWIR optical fiber for generating miniature point source.

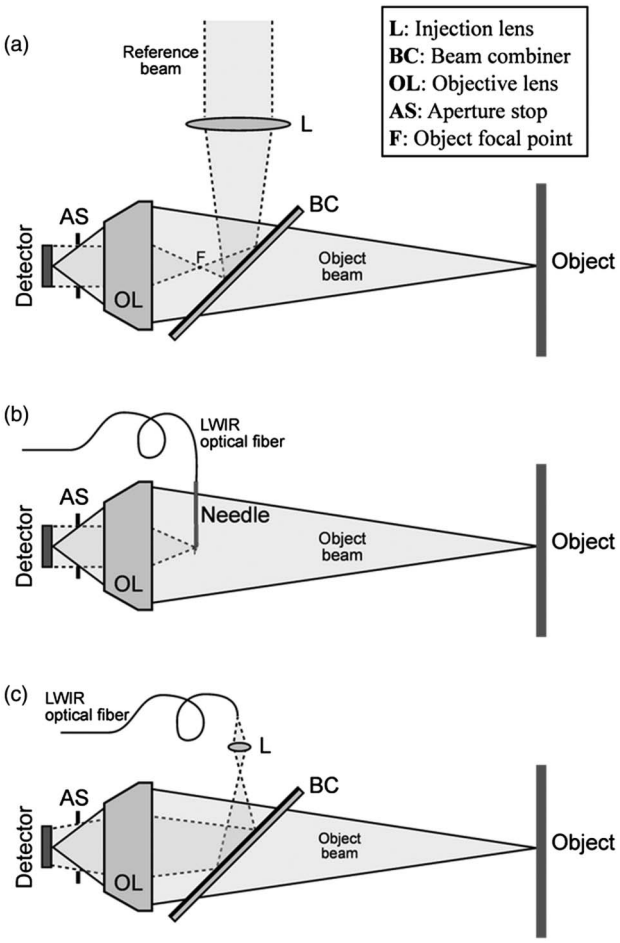

Fig. 4. Various schemes for reference beam injection: (a) with focusing reference beam at front focal point through BC, (b) with modified needle at front focal point, (c) through BC and reference launch with fiber and lens beyond the focal point.

The BC in the schemes in Figs. 4(a) and 4(c) is a wedged ZnSe plate with ratio R50/T50, which is insensitive to polarization. In order to avoid vignetting, the BC has a 80 mm diameter, which is not an advantage in compactness compared to the needle.

The different setups described above have their pros and cons, and we selected one for further development of a mobile instrument. The needle solution [Fig. 4(b)] has the advantage of allowing very compact setup and is cheaper than a BC. However, the alignment into the fiber is difficult because of the invisible wavelength. We experienced problems of melting of the fiber input when slight misalignment occurs. Moreover, the fiber being multimode, the reference beam exhibits speckles at the fiber output. These speckles can move if the fiber is not well stabilized mechanically and can prevent interference with the object beam. The first system with the BC [Fig. 4(a)] allows a stiffer setup without misalignment problem. The drawback of the R50/T50 BC is that half of the light intensity is lost in the object beam, which requires more laser power for object illumination. The third system [Fig. 4(c)] suffers from the same constraints related to the fiber as well as losses due to the BC. Consequently, this is the least interesting scheme for reference injection. Finally, for building a mobile instrument for field applications, the scheme depicted by Fig. 4(a) is our best choice.

Despite this choice, we have tried all these setups in NDT experiments with actual samples made of composites, and the results presented in the next section have to be understood rather for illustration than for deep comparison between reference injection system performances.

C. Results

For the investigation, we used a series of composite samples made of various skin materials, mainly CFRP and Kevlar, with various layers and defects of different natures and depths underneath the surface. Figure 5 shows photographs and definition of samples we used for the different results shown later. Sample 1 [Fig. 5(a)] has a rectangular shape of 36 cm × 30 cm. It is made of CFRP layers arranged in four vertical zones with increasing thickness. A cross section along the sample thickness is shown under the picture. The first zone on the left has three layers with total thickness of typically 0.9 mm. Going to the right, the second zone has six layers, the third one nine layers, and the last one on the right 12 layers, with a final thickness of 3.5 mm. This sample has no defect. Sample 2 [Fig. 5(b)] has a square shape of 25 cm × 25 cm with a thickness of 4 mm and is also made of CFRP layers. A delamination provoked by an impact is present (grey dots). Sample 3 [Fig. 5(c)] has the same rectangular shape and lateral extent as sample 1 with four vertical zones. However, the sample has an 18 mm thick Rohacell core sandwiched between two Kevlar skins. As shown in the cross section along the thickness, the upper skin has the same geometry as for sample 1 while the bottom skin has an overall thickness of three layers. The Rohacell core is glued on the two skins, and defects were included between the upper skin and the core. Their location is superposed on the picture: each vertical zone has two debondings (black dots) of various sizes, cracked core (grey dots) of various sizes, and two surface cracks (grey lines).

For all these samples, the surface roughness was similar to or larger than the wavelength; therefore speckle was naturally present and no further surface painting was necessary. These samples were used in a typical NDT application where thermal stress is applied and the sample mechanical response (deformation) is observed. The thermal stresses are provoked by halogen or infrared lamps. In practice, a series of phase-shifted specklegrams is recorded before heating the sample. Then the lamp is switched on for a few tens of seconds. Afterwards it is switched off and one waits a few tens of seconds to record new phase-shifted specklegrams. The phase difference between the actual deformed state and the reference one (before heating) is then computed in real time and is related to the deformation, as explained in

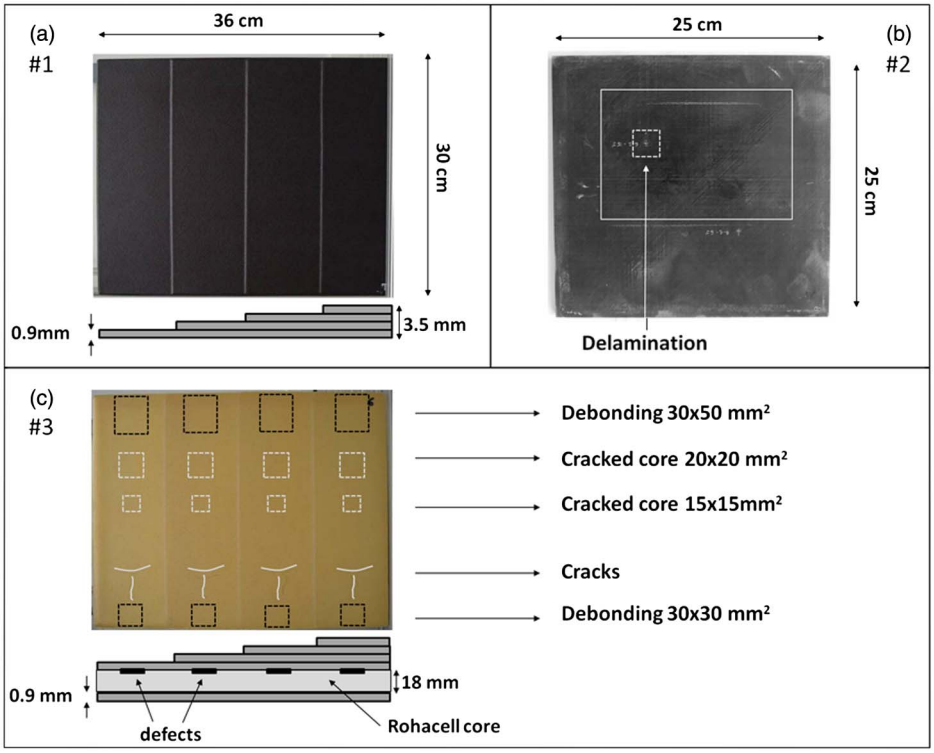

Fig. 5. (Color online) Photographs and definition of the different samples used in our experiments.

Section 2.A. Figure 6(a) shows the deformation of sample 1. The entire object is imaged: it was placed at a distance of typically 1.3 m from the and was illuminated by a lens with 25.4 mm focal length. The pattern shows shifts in fringes between the different zones. The ESPI setup made use of the injection scheme depicted in Fig. 4(a). Figure 6(b) is obtained using the injection setup with the needle depicted in Fig. 4(b) and with sample 2. In this case, the object was placed at around 70 cm from the OL and was illuminated by a negative lens with −20 mm focal length. The total observed area is 20 cm × 15 cm and is represented by a rectangle in Fig. 5(b). The delamination is well identified by a strong local deformation under the thermal stress. Figure 6(c) is obtained using the injection setup with the fiber depicted in Fig. 4(c) and sample 3. In this case the object distance and illumination lens are the same as for sample 1. The overall deformation is seen as large circular fringes, whereas defects can be seen as local fringe patterns or tiny variations of phase in some places. Figure 6(d) shows the postprocessing of Fig. 6(c), where the global deformation has been eliminated. The process consists of phase unwrapping of the phase map in Fig. 4(c), fitting the result with a two-dimensional (2D) second-degree polynomial and subtracting it from the phase. The remainder is the contribution of local deformation induced by defects. It must be noted that samples 1 and 3, which are observed at 1.3 m distance from the sensor, were placed out of the table where the remaining part of the optical setup was lying. Moreover, the samples were not firmly attached or clamped but rather were simply standing in a overall vertical position, with simply two pillars on the back side keeping the sample in place.

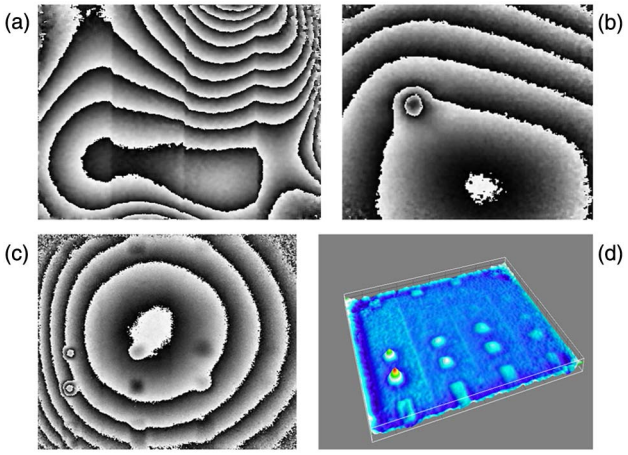

Fig. 6. (Color online) (a)–(c) Phase maps modulo 2π obtained after heating composite samples. (d) Defect map after postprocessing phase map (c).

Figure 7 shows the effect of using a higher wavelength and the interest of using LWIR wavelengths. Figure 7(a) was obtained on sample 2 with the setup of Fig. 4(c), a CO_2 laser with 9.3 μm wavelength and with 60 s heating of sample. The change of wavelength is due to the fact that the previous laser at 10.6 μm was no longer available. Nevertheless, as the response of microbolometer arrays is almost identical for both lines, results are comparable with those obtained at 10.6 μm. Figures 7(c) and 7(d) show

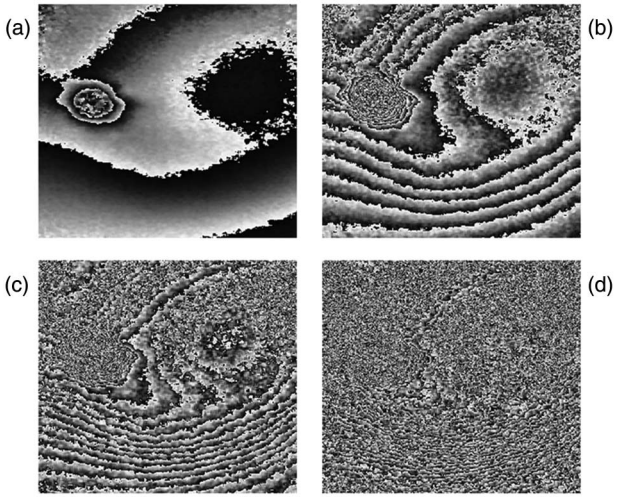

Fig. 7. (a) Phase map modulo 2π obtained by ESPI at micrometer wavelength. (b)–(d) Simulated equivalent phase map with shorter wavelengths, respectively 1.85, 0.93, and 0.46 μm.

how the result of the same deformation of Fig. 7(a) would have looked if shorter wavelengths were used. The figures were obtained by simple computation, noting that, for a given displacement and setup, the product $\boldsymbol{s}\cdot\boldsymbol{d}$ in Eq. (2) is conserved. Therefore changing the wavelength λ allows computing new modulo 2π phase maps. Figures 7(b), 7(c), and 7(d) are obtained respectively with 1.85, 0.93, and 0.46 μm wavelength, and the latter is close that which should be observed with a usual visible ESPI system. Equivalent large displacements could be measured by using interferometers based on visible radiation, but in this case many more specklegrams should be recorded during the object deformation (e.g., by using a high-speed camera) and consecutive addition of the phases is necessary. This approach is time consuming and increases the errors due to the addition of phase maps.

3. LWIR Off-Axis DHI

A. Setup and Technique Description

The setup used for DHI is very similar to the one for ESPI (see Fig. 1); the only difference is the off-axis configuration that allows obtaining the phase of the object wavefront without using a phase shifter. This configuration is obtained experimentally by adding a small angle between the reference and object beams. The DHI method consists in recording the interference of reference and object waves by the matrix sensor, here the microbolometer array of the camera. The recorded intensity function can described by Eqs. (1a) and (1b) and is called here hologram, whereas we named it a specklegram in Section 2.A. The fourth term of Eq. (1a) contains the information about the object wavefront amplitude. Digital holography consists in numerically reconstructing the object wavefront from the recorded pattern. We are restricted by the spatial resolution of the detector, and for recording the digital hologram, the spatial frequency f should satisfy the sampling condition $<1/(2\Delta)$, where Δ is the camera pixel size, in order to ensure a correct spatial sampling of the hologram [27].

In the case of the off-axis configuration, a 2D spatial Fourier transform of the recorded intensity allows separating the $+1$ order $\boldsymbol{R}^*(x,y)\boldsymbol{U}(x,y)$ from the other terms described in Eq. (1a) [28]. According to definition of phases given in Section 2.A, the phase difference between two wavefronts $\boldsymbol{U_a}$ and $\boldsymbol{U_b}$ recorded at different instants is expressed as

$$\begin{aligned}\Delta\phi &= \phi_a - \phi_b = \varphi_R - \varphi_{Ua} - (\varphi_R - \varphi_{Ub}) \\ &= \tan^{-1}\left[\frac{\mathrm{Im}(\boldsymbol{R}^*\boldsymbol{U}_b)}{\mathrm{Re}(\boldsymbol{R}^*\boldsymbol{U}_b)}\right] - \tan^{-1}\left[\frac{\mathrm{Im}(\boldsymbol{R}^*\boldsymbol{U}_a)}{\mathrm{Re}(\boldsymbol{R}^*\boldsymbol{U}_a)}\right], \qquad (4)\end{aligned}$$

where Re and Im denote respectively the real and imaginary part of the signal and where dependency to coordinates (x,y) has been omitted for clarity. The phase difference computed by Eq. (3) can be related to the object displacement d in every point through Eq. (2), similarly to ESPI. The advantage of this method is that only a single hologram is necessary for the wavefront phase calculation, as opposed to ESPI or in-plane DHI, for which all the terms of Eq. (1a) are spatially superposed. This requires the phase-shifting method to be applied by capturing multiple images, hence imposing stability of the object during capture. The DHI technique presented here is thus well suited for the investigation of dynamic processes.

This advantageous configuration has a limitation that comes from the above mentioned sampling condition. Indeed, the frequency f is given by $f = 1/d_f = [\sin(\theta_{\mathrm{ref}}/2) + \sin(\theta_{\mathrm{obj}}/2)]/\lambda$, with d_f the distance between adjacent maxima and minima of an interference fringe on the detector and θ_{ref} and θ_{obj} respectively the angles that the reference and object beams make with the normal of the detector. Therefore these angles must be rendered as small as possible by limiting the aperture of the optical system.

The camera AS located between the OL and the sensor was used to restrict the spatial frequency of the object beam. In order to estimate the aperture size suitable for digital holography, the whole system (OL, AS, and microbolometer array sensor) was simulated by using ZEMAX ray tracing software; this led us to choose an aperture size of 4 mm, which is small compared with the maximal aperture, which has a diameter 21 mm. Because reducing this aperture is not possible with such a thermographic system (fixed diameter), we manufactured a thin aperture on a thick black paper sheet that was then attached on the open position of the camera aperture wheel. By choosing the small aperture, we reduce the image resolution and the intensity recorded by the detector. The reference beam was focused through the objective in the plane of the aperture. Reducing the aperture has the negative effect of reducing at the same time the intensity at the detector and

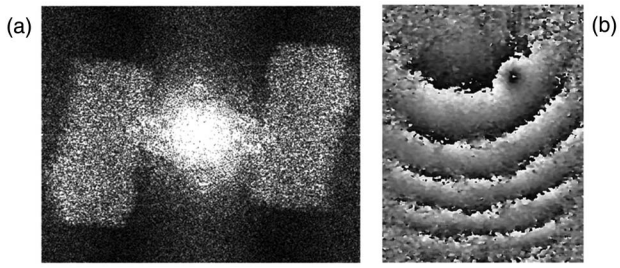

Fig. 8. DHI method. (a) Reconstructed digital hologram. (b) Phase difference due to the thermal deformation.

the spatial resolution of the reconstructed object wave. Nevertheless, we managed to obtain results, which are presented in the next section.

B. Results

Figure 8(a) shows the modulus of the Fourier transform of the recorded intensity. The central peak is the zero order containing information about reference and object beam intensities according to Eq. (1). The two first orders (containing information on the object wave field $\boldsymbol{U}$ and its conjugate $\boldsymbol{U}^*$) are also visible. A similar digital hologram is reconstructed with the deformed object. The phase variation due to the deformation, described by Eq. (4), can be computed. Figure 8(b) shows the phase map due to heating of sample 2, placed at typically 70 cm from the OL and illuminated by a negative lens with −20 mm focal length, giving a total observed area of 20 cm × 15 cm. Because of the small aperture, the resolution of the recorded images and the quality of the phase difference is lower than the ones obtained with ESPI. Despite the lower quality, DHI requires only a single acquisition per object state and not a set of phase-shifted ones. Therefore, DHI could be used for analysis of large dynamic displacement measurements as an alternative to ESPI, which is used for slower-speed phenomena.

4. LWIR DS

Shearography is usually used for investigation of strain [29], and mobile systems are nowadays used increasingly in industries for inspection in view of flaw detection [30]. Shearography does not make use of the interference of reference and object waves, contrary to both previous methods. Instead, a single beam coming from the laser is used to illuminate the object, which scatters light towards the observation system, which is preceded by a shearing device. In literature one can find various configurations of shearing devices. They can be based on (1) insertion of a wedged glass plate in half of the field of view [29], (2) birefringent elements introducing polarization separation in images followed by a polarizer [31], or (3) a modified Michelson interferometer [29]. For our demonstration, we used the Michelson configuration because this is the easiest to put in place with LWIR optical components. Figure 9(a) shows the scheme of the setup. The BC is polarization insensitive and has ratio R50/T50. It splits the image into two similar,

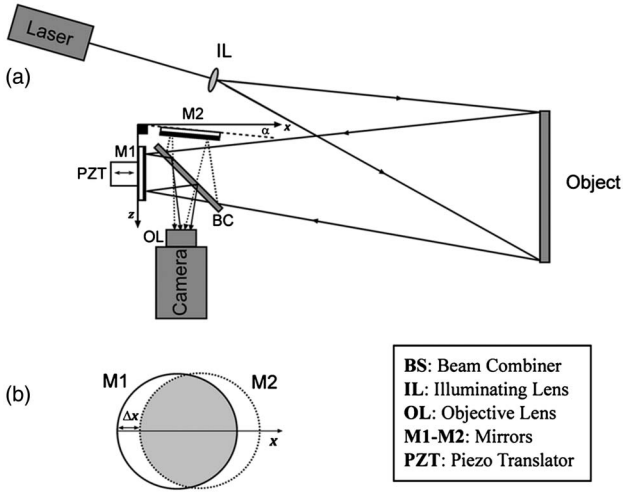

Fig. 9. (a) Shearography setup. (b) Overlap of images reflected by mirrors M1 and M2 with lateral shear along x direction and amount Δx.

equal-intensity images, the transmitted one (represented by solid lines) and the reflected one (represented by dotted lines), which are reflected by mirrors, respectively M1 and M2, to be further recombined at the level of the camera. One of the two mirrors (M2) is tilted by an angle α, which allows producing a lateral shear between the two images. Figure 9(b) shows the situation where the shear is oriented along direction x. However, shear direction can be adjusted in the image plane (x,y). Interference occurs where the two images overlap [grey zone in Fig. 9(b)], and the intensity of the interference pattern is described by a function identical to Eqs. (1a) and (1b) except that $\boldsymbol{R}(x,y)$ and $\boldsymbol{U}(x,y)$ are replaced respectively by the object field $\boldsymbol{U}(x,y)$ and itself laterally displaced (or sheared), $\boldsymbol{U}(x+\Delta x, y+\Delta y)$, where Δx and Δy are shear amounts respectively along the x and y directions.

The strain of object (along the x direction) is related to the phase difference by [29]

$$\Delta\phi = \frac{2\pi}{\lambda}\boldsymbol{s}\frac{\partial \boldsymbol{d}}{\partial x}\Delta x, \tag{5}$$

where $\boldsymbol{s}$ is the sensitivity vector and $\partial \boldsymbol{d}/\partial x$ and Δx are respectively the strain component and the shear amount in the x direction. A piezoelectric translator was set in one path of the interferometer to shift the path length, and a four-step algorithm was used to calculate the phase. One of the main applications of shearography in NDT is the detection of defect where the latter is seen as a local variation of strain. As for ESPI [Fig. 6(b)] and DHI shown previously, the investigated object is sample 2 with the same setup parameters (object distance and IL). Figure 10 shows the phase map, where the delamination defect underneath the surface is clearly detected. The process of the measurement is identical to phase-shifting ESPI presented in Section 2.A: a series of phase-shifted shearograms (instead of specklegrams) are recorded

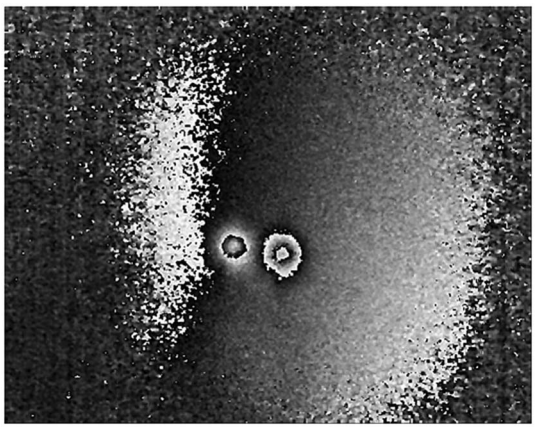

Fig. 10. Phase map obtained with LWIR shearography after heating of CFRP sample.

when the sample is at rest, and the phase ϕ_a is calculated by the four-bucket algorithm. Afterwards the sample is heated, for instance by a halogen lamp, for a few seconds, and then the heat source is switched off. During the temperature relaxation that follows, a series of phase-shifted specklegrams are again recorded, giving new phase ϕ_b. The phase difference between ϕ_b and ϕ_a is then computed, which shows the strain of the sample between the initial and stressed states following Eq. (5).

5. Discussion

Measuring displacement and deformation of composites is a topic of interest for aeronautical industries, either for analyzing their behavior under various types and magnitudes of stresses or for detecting local defects by abnormal local deformation induced by the defect when the sample undergoes stress (usually thermal). If we want to discuss the advantages and drawbacks of the techniques presented in this paper, we have to put them in perspective with currently used NDT techniques.

Usual noncontact optical NDT techniques involve either methods based on coherent light or noncoherent light. In the first category one finds methods like ESPI and shearography, which are used for full-field displacement or strain measurements, respectively. Their measurement resolution is related to the wavelength of the laser. In the second category one finds three-dimensional coordinate measurements such as fringe projection [32], stereocorrelation [32,33], or videogrammetry [32]. In this case, the displacements or the strains are obtained by capture of coordinates of the sample surface points at different instants of the stress and by computing numerical subtraction. Their measurement resolution depends mainly on the resolution of the camera and is a fraction of the volume observed. As a good rule of thumb, one can say that a megapixel camera offers a resolution of 1/1000 of the object size, with equivalent performance in term of displacement.

The noncoherent techniques are used in thermomechanical analyses or structural tests where the mechanical displacements or strain of composite parts are monitored as a function of stresses. Usually these parts have dimensions similar to the ones considered in our study (a few tens of centimeters wide) or even higher (meters wide). Therefore resolutions are on the order of a few hundred of micrometers. Better resolutions can be obtained but require stability and multiple image acquisitions [32], which is not an advantage. Because of their noninterferometric character, these methods have the advantage of being quite immune to environmental perturbations. An important drawback is that surfaces have to be prepared prior to measurements. For instance, stereocorrelation requires spraying the surface with a white color superposed by a random pattern of black dots whereas videogrammetry requires retroreflecting targets glued on some surface points. In the last case, this strongly limits the lateral sampling of the object. Despite this, these techniques are used in a wide variety of structural tests, with very high displacements or deformations and high temporal dynamics as in shocks or rupture (destructive) tests.

For displacement measurement with higher resolution, ESPI can be used, but as the wavelength is short, maximum displacements remain limited to a few micrometers with resolutions of a few tens of nanometers. For displacements that are too high for the range of visible ESPI (because fringes are not resolved anymore), one needs to record a very large number of specklegrams and compute their phase differences $\Delta\phi$, which allow a resolvable number of fringes, before adding these subsequent $\Delta\phi$ for obtaining the entire displacement. This is both time consuming and increases the measurement errors. Another drawback is that visible interferometric techniques are generally used in laboratories where quiet environmental conditions are present.

The LWIR ESPI techniques discussed in this paper clearly have the advantage of filling a gap between the high resolution allowed by visible ESPI and the low resolutions of noncoherent techniques. A few hundreds of micrometers can be reached with LWIR ESPI in a single shot, whereas the equivalent measurement would require 20 times more images in the visible range. Also the experiments were performed with samples located outside of the optical table where the LWIR setup was placed, and moreover they were not stiffly attached. This is an encouraging indication for the possibility of future development of a mobile instrument for out-of-laboratory applications.

Concerning the dynamics of the phenomena of interest, the phase-shifting recording sequence duration (typically 0.5 s) limits the velocities of displacements to a few micrometers per second (considering that the phase-shifting objects do not move by a fraction of the wavelength during the recording sequence). This is still 20 times better than for the visible ESPI technique.

Typical applications addressed by LWIR ESPI are the thermomechanical assessment of composites, for

instance measuring the deformation of coupons or elements of larger sizes like the ones of the study. In these cases the samples may undergo a few tens of degrees of temperature variations and/or large mechanical stresses, like those experienced either by fuselage or wing parts in the different sequences of flight, or in some parts of engines. Another application is the detection of defects, as was shown with some samples, but this requires additional postprocessing for removing the large global deformation as was shown in Figs. 6(c) and 6(d).

Concerning LWIR DHI, as already mentioned, faster phenomena can be monitored compared to LWIR ESPI. Indeed, single-shot measurements are possible with recording time related to the frame rate of microbolometer, say 1/50 of a second. Despite the lower lateral resolution of the off-axis DH configuration and the lower quality of interferograms reported (which in turn limits the maximum displacement resolvable), millimeter-per-second-velocity phenomena seem reasonable to achieve. This opens the way to vibration measurement or dynamic stresses like in some structural testing (such as fatigue).

Shearography in visible light is mostly used for internal defect detection like delaminations in composite laminates and debondings between composite skins and other structural elements. Such defects induce local strain under given stresses, like heating with a lamp, vibration by a piezoactuator, and so forth. Identifying the location of these locally higher-strain areas provides instant and easy position and extent of the defects underneath the surface. LWIR shearography showed the same typical results as those obtained by visible shearography, but here strains are 20 times higher. This means than larger stresses need to be applied for the same results, which is not necessarily an advantage. Due to the fact that the equipment of the LWIR shearography setup is more cumbersome than in the visible range, LWIR shearography should have limited interest for defect detection. However, it would keep the advantage of filling the gap between visible shearography and noncoherent techniques for the measurement of full-field strain images.

6. Conclusion: Future Prospects

We have shown that it is possible to extend various interferometric NDT techniques (currently applied with visible lasers) to the LWIR spectral range, associating state-of-the-art thermographic cameras with microbolometer arrays and CO_2 lasers. We have presented different developments at the level of the optical setup. One critical point is the injection of the reference beam into the camera with its OL attached. Several schemes were studied and implemented for ESPI and DHI. We also have demonstrated the feasibility of LWIR shearography, which does not require an external reference beam. In all cases we performed typical NDT experiments on the basis of composite parts with size, materials, and defects that are representative of aeronautical applications.

The sensitivity-to-displacements measurement of LWIR interferometric NDT techniques is situated between the one of their visible light counterparts and the one of another category of NDT techniques working with noncoherent light. Therefore we now fill a gap between two measurement ranges that do not overlap. Another advantage of using LWIR for interferometric techniques is that the latter could be used in more perturbed environmental conditions due to the low sensitivity to phase variations between reference and object beams. The disadvantage of longer wavelength is that the resolving power in term of imaging is 20 times lower, but this is not a real problem for object sizes larger than centimeters, as considered in our applications.

The results presented in this paper are initial laboratory developments for a future mobile system. The most promising technique is LWIR ESPI, which gives the best results and will be implemented for thermomechanical analyses and defect detection in composites.

These works are funded by the FP7 European project FANTOM (ACP7-GA-2008-213457).

References

1. C. M. Vest, *Holographic Interferometry* (Wiley, 1979).
2. R. Jones and C. Wykes, *Holographic and Speckle Interferometry* (Cambridge University, 1989).
3. P. W. Kruse, *Uncooled Thermal Imaging. Arrays, Systems and Applications* (SPIE, 2001).
4. B. Fièque, P. Robert, C. Minassian, M. Vilain, J. L. Tissot, A. Crastes, O. Legras, and J. J. Yon, "Uncooled amorphous silicon XGA IRFPA with 17 μm pixel-pitch for high end applications," Proc. SPIE **6940**, 69401X (2008).
5. J. S. Chivian, R. N. Claytor, and D. D. Eden, "Infrared holography at 10.6 μm," Appl. Phys. Lett. **15**, 123–125 (1969).
6. W. A. Simpson and W. E. Deeds, "Real-time visual reconstruction of infrared holograms," Appl. Opt. **9**, 499–501 (1970).
7. S. Kobayashi and K. Kurihara, "Infrared holography with wax and gelatin film," Appl. Phys. Lett. **19**, 482–484 (1971).
8. R. R. Roberts and T. D. Black, "Infrared holograms recorded at 10.6 μm and reconstructed at 0.6328 μm," Appl. Opt. **15**, 2018–2019 (1976).
9. M. Rioux, M. Blanchard, M. Cornier, R. Beaulieu, and D. Bélanger, "Plastic recording media for holography at 10.6 μm," Appl. Opt. **16**, 1876–1879 (1977).
10. R. Beaulieu, R. A. Lessard, M. Cormier, M. Blanchard, and M. Rioux, "Infrared holography on commercial wax at 10.6 μm," Appl. Phys. Lett. **31**, 602–603 (1977).
11. R. Beaulieu, R. A. Lessard, M. Cormier, M. Blanchard, and M. Rioux, "Pulsed IR holography on takiwax films," Appl. Opt. **17**, 3619–3621 (1978).
12. J. Lewandowski, B. Mongeau, and M. Cormier, "Real time interferometry using IR holography on oil films," Appl. Opt. **23**, 242–246 (1984).
13. R. Beaulieu, R. A. Lessard, and S. L. Chin, "Resist recording media for holography at 10.6 mm," Proc. SPIE **2042**, 259–263 (1994).
14. R. Beaulieu and R. A. Lessard, "Infrared holography on poly(acrylic acid) films," Proc. SPIE **4087**, 1298–1301 (2000).
15. U. Schnars and W. Jüptner, "Direct recording of holograms by a CCD target and numerical reconstruction," Appl. Opt. **33**, 179–181 (1994).
16. O. J. Løkberg and O. Kwon, "Electronic speckle pattern interferometry using a CO_2 laser," Opt. Laser Technol. **16**, 187–192 (1984).

17. E. Allaria, S. Brugioni, S. De Nicola, P. Ferraro, S. Grilli, and R. Meucci, "Digital holography at 10.6 μm," Opt. Commun. **215**, 257–262 (2003).
18. S. De Nicola, P. Ferraro, S. Grilli, L. Miccio, R. Meucci, P. K. Buah-Bassuah, and F. T. Arecchi, "Infrared digital reflective-holographic 3D shape measurements," Opt. Commun. **281**, 1145–1449 (2008).
19. N. George, K. Khare, and W. Chi, "Infrared holography using a microbolometer array," Appl. Opt. **47**, A7–A12 (2008).
20. J.-F. Vandenrijt and M. Georges, "Infrared electronic speckle pattern interferometry at 10 μm," Proc. SPIE **6616**, 6616–6672 (2007).
21. J.-F. Vandenrijt and M. Georges, "Electronic speckle pattern interferometry with microbolometer arrays at 10.6 μm," Appl. Opt. **49**, 5067–5075 (2010).
22. I. Yamaguchi, "Fundamentals and applications of speckle," Proc. SPIE **4933**, 1–8 (2003).
23. J.-F. Vandenrijt, C. Thizy, I. Alexeenko, I. Jorge, I. López, I. S. de Ocáriz, G. Pedrini, W. Osten, and M. Georges, "Electronic speckle pattern interferometry at long infrared wavelengths: scattering requirements," in *Fringe 2009—6th International Workshop on Advanced Optical Metrology*, W. Osten and M. Kujawinska, eds. (Springer, 2009), pp. 596–599.
24. I. Alexeenko, J.-F. Vandenrijt, M. P. Georges, G. Pedrini, T. Cédric, W. Osten, and B. Vollheim, "Digital holographic interferometry by using long wave infrared radiation (CO_2 laser)," Appl. Mech. Mater. **24–25**, 147–152 (2010).
25. T. Maack, R. Kowarschik, and G. Notni, "Optimum lens aperture in phase-shifting speckle interferometric setups for maximum accuracy of phase measurement," Appl. Opt. **36**, 6217–6224 (1997).
26. J.-F. Vandenrijt, "Etude et développment de techniques de métrologie de déplacements en lumière cohérente en infrarouge thermique," Ph.D. dissertation (Université de Liège, 2010) (in French).
27. G. Pedrini and H. Tiziani, in *Digital Speckle Pattern Interferometry and Related Techniques*, P. K. Rastogi, ed. (Wiley, 2001).
28. M. Takeda, Hideki, and S. Kobayashi, "Fourier-transform method of fringe pattern analysis for computer-based topography and interferometry," J. Opt. Soc. Am. **72**, 156–160 (1982).
29. W. Steinchen and L. Yang, in *Digital Shearography* (SPIE, 2003).
30. M. Kalms and W. Osten, "Mobile shearography system for the inspection of aircraft and automotive components," Opt. Eng. **42**, 1188–1196 (2003).
31. S. Debrus, "Speckle shearing interferometer using a Savart plate," Opt. Commun. **20**, 257–267 (1977).
32. F. Chen, G. M. Brown, and M. Song, "Overview of the three-dimensional shape measurement using optical methods," Opt. Eng. **39**, 10–22 (2000).
33. M. A. Sutton, J.-J. Orteu, and H. W. Schreier, *Image Correlation for Shape, Motion and Deformation Measurement. Basic Concepts, Theory and Applications* (Springer, 2009).